Interstitial oxide ion conductivity in the layered tetrahedral network melilite structure

XIAOJUN KUANG[1], MARK A. GREEN[2,3], HONGJUN NIU[1], PAWEL ZAJDEL[2,4], CALUM DICKINSON[1], JOHN B. CLARIDGE[1], LAURENT JANTSKY[1] AND MATTHEW J. ROSSEINSKY[1]*

[1] Department of Chemistry, The University of Liverpool, Liverpool, L69 7ZD, UK
[2] NIST Center for Neutron Research, National Institute of Standards and Technology, Gaithersburg, Maryland 20899, USA
[3] Department of Materials Science and Engineering, University of Maryland, College Park, Maryland 20742-2115, USA
[4] Department of Chemistry, University College London, 20 Gordon Street, London W1X 0AJ, UK
*e-mail: rossein@liv.ac.uk

High-conductivity oxide ion electrolytes are needed to reduce the operating temperature of solid-oxide fuel cells. Oxide mobility in solids is associated with defects. Although anion vacancies are the charge carriers in most cases, excess (interstitial) oxide anions give high conductivities in isolated polyhedral anion structures such as the apatites. The development of new families of interstitial oxide conductors with less restrictive structural constraints requires an understanding of the mechanisms enabling both incorporation and mobility of the excess oxide. Here, we show how the two-dimensionally connected tetrahedral gallium oxide network in the melilite structure $La_{1.54}Sr_{0.46}Ga_3O_{7.27}$ stabilizes oxygen interstitials by local relaxation around them, affording an oxide ion conductivity of 0.02–0.1 $S\,cm^{-1}$ over the 600–900 °C temperature range. Polyhedral frameworks with central elements exhibiting variable coordination number can have the flexibility needed to accommodate mobile interstitial oxide ions if non-bridging oxides are present to favour cooperative network distortions.

Oxide ion electrolytes with specific conductivities exceeding $10^{-2}\,S\,cm^{-1}$ at low (≈500 °C) temperatures are required for solid-oxide fuel cells[1–3]. The mobile oxide species are usually vacancies on the anion sublattice[2–4], but recently there has been growing interest in systems where excess oxide ions (interstitials) carry the charge. Mixed electronic and ionic conduction involving mobile interstitial oxide ions is found in the layered perovskites La_2NiO_{4+x} (ref. 5), scheelite $CeNbO_{4+x}$ (ref. 6), $Bi_2Sr_2CaCu_2O_{8+x}$ (ref. 7) and fluorite UO_{2+x} (ref. 8). Pure oxide ion conduction by interstitial anions is rare, for example, it is found in the family of $La_{10-x}(MO_4)_6O_{3-1.5x}$ (M = Si, Ge) apatite-structured materials[9–12] (for example, $\sigma \sim 0.01$–$0.06\,S\,cm^{-1}$ over the 600–900 °C range in $La_{9.75}Sr_{0.25}(SiO_4)_6O_{2.895}$ (ref. 13)), the scheelite $La_{0.2}Pb_{0.8}WO_{4.1}$ (ref. 14) (for example, $\sigma \sim 0.007$–$0.07\,S\,cm^{-1}$ at 600–900 °C) and mayenite $Ca_{12}Al_{14}O_{33}$ (ref. 15) ($\sigma \sim 10^{-4}$–$0.01\,S\,cm^{-1}$ at 500–1,200 °C). The apatite is a promising oxide electrolyte candidate for solid-oxide fuel cells as its high oxygen transport number (>0.9) is maintained over a wide (1–10^{-21} atm) oxygen partial pressure range[13]. Silicate apatites have conductivities comparable to those of yttrium-stabilized ZrO_2 (YSZ), with even higher conductivity found for germanate apatites[12]. These pure interstitial oxide ion conductors are all based on tetrahedral oxyanions—apatite and scheelite have isolated anions, whereas the three-dimensional (3D) corner-sharing network structure of mayenite[16] differs as the interstitial oxygen is bound to extra-framework Ca^{2+}. The local mechanism by which excess oxygen can be accommodated in the isolated tetrahedral anion materials has been identified for the apatites by lattice dynamics calculations and structural and NMR studies—excess oxygen transforms $(Si/Ge)O_4$ to $(Si/Ge)O_5$ units because of the rotational flexibility of isolated tetrahedra[10,11,17,18]. Isolated complex anion structures with variable coordination number are rare, so it is important to identify how mobile interstitial oxide ions can be introduced into more common structure types based on linked polyhedra. The demonstration here that the 2D extended corner-sharing tetrahedral network of the melilite $La_{1+x}Sr_{1-x}Ga_3O_{7+0.5x}$ can both accommodate excess oxide anions and sustain their mobility opens up many new structural families of materials as candidate interstitial oxide conductors.

$LaSrGa_3O_7$ adopts the melilite structure, which consists of alternating cationic $(La/Sr)_2$ and corner-sharing tetrahedral anionic Ga_3O_7 layers and features five-fold tunnels that accommodate the eight-coordinate La/Sr as chains of cations[19]. It is an insulator and is found as a secondary phase in the synthesis of the Sr, Mg-doped $LaGaO_3$ (LSGM) electrolyte[20]. Rozumek *et al.*[21,22] showed that the La/Sr ratio in the $LaSrGa_3O_7$ melilite phase can be extended to $La_{1.6}Sr_{0.4}$, which afforded a high conductivity of $\sim 0.1\,S\,cm^{-1}$ at 950 °C with an oxygen transport number of 0.80–0.95 above 600 °C. Rozumek *et al.*[21,22] proposed a range of candidate defect models, favouring an oxygen-deficient model. On the contrary, Raj *et al.*[23] reported that the La/Sr ratio for this solid solution can only be extended to $La_{1.05}Sr_{0.95}Ga_3$ without the formation of Sr-doped $LaGaO_3$ perovskite (LSG) impurity, with a maximum oxide ion conductivity of $\sim 10^{-3}\,S\,cm^{-1}$ at 950 °C.

The composition and electrical performance of this solid solution are thus controversial. Precise phase compositions (see Supplementary Information, Fig. S1) are needed to identify mechanisms for the introduction of ionic charge carriers. The starting cation composition $La_{1+x}Sr_{1-x}Ga_3$ for $x < 0.6$ resulted in a mixture of a melilite phase (with cell parameters differing from the parent $LaSrGa_3O_7$) and a second phase, LSG perovskite. The cell parameters of the melilite phases obey Vegard's law for $0 \leq x \leq 0.6$ (see Supplementary Information, Fig. S3). A single-phase material of composition $La_{1.54}Sr_{0.46}Ga_3O_{7.27}$ was obtained by reaction at 1,200 °C for 12 h and 1,400 °C for 12 h of a starting material with cation ratios $La_{1.54}Sr_{0.46}Ga_{3.05}$—the 1.7 mol% excess of Ga compensates for volatilization during the reaction to suppress the formation of the competing LSG phase. Energy-dispersive spectroscopy (EDS) elemental analysis in the transmission electron microscope showed a homogeneous cationic ratio of $La_{1.58}Sr_{0.52}Ga_3$, compared with $La_{1.01}Sr_{0.99}Ga_3$ found by EDS for the parent $LaSrGa_3O_7$ phase. Both materials were phase-pure by EDS. These results agree well with the nominal composition within the expected errors, and are consistent with the composition $La_{1.51}Sr_{0.43}Ga_3$ found from inductively coupled plasma (ICP) elemental analysis. The existence of the single-phase melilite material $La_{1.54}Sr_{0.46}Ga_3O_{7.27}$, where the oxygen content is inferred by the need to balance the charges, confirms the existence of a $La_{1+x}Sr_{1-x}Ga_3$ solid solution deduced from the multiphase samples.

The electrical properties of $La_{1.54}Sr_{0.46}Ga_3O_{7.27}$ were measured by a.c. impedance spectroscopy on ceramic pellets with 96% of the theoretical X-ray density. Impedance data at <500 °C exhibit a significant Warburg electrode response[24,25] with an associated large capacitance ($>10^{-7}$ F cm^{-1}) in the low-frequency range (<10 Hz), which is diagnostic of ionic conduction with partially blocking electrodes—the bulk and grain boundary responses at higher frequencies overlap to exhibit part of an asymmetric semicircular arc, (Fig. 1a; Supplementary Information, Fig. S4), showing that $La_{1.54}Sr_{0.46}Ga_3O_{7.27}$ exhibits typical ionic conduction behaviour. The intercept of the semicircular arc at low frequency was extracted as the total resistivity $R_b + R_{gb}$. Above 500 °C, the electrode response dominated the impedance data and gradually collapsed to a semicircular arc; the intercept at high frequency was extracted as the total resistivity. High-temperature four-probe d.c. data (500–1,000 °C) give effectively identical conductivity values (see Supplementary Information, Fig. S5), validating the impedance data analysis because the four-probe data do not include an electrode–electrolyte contribution[26].

The Arrhenius plot of the total conductivity of $La_{1.54}Sr_{0.46}Ga_3O_{7.27}$ measured in air is shown in Fig. 1c. From 600 to 900 °C, this material shows a high total conductivity of 0.02–0.1 S cm^{-1}, in agreement with Rozumek *et al.*[22]. This conductivity is slightly lower at above 600 °C than that of LSGM (for example, $La_{0.8}Sr_{0.2}Ga_{0.83}Mg_{0.17}O_{2.815}$ (ref. 20)), Gd-doped ceria (GDC) (for example, $Ce_{0.9}Gd_{0.1}O_{1.95}$ (ref. 27)) and the germanate apatite ($La_{9.5}(Ge_{5.5}Al_{0.5}O_{24})O_2$ (ref. 12)), but is higher than those for the silicate apatites and YSZ (Fig. 1d). Below 600 °C, the conductivity of $La_{1.54}Sr_{0.46}Ga_3O_{7.27}$ is slightly higher than that of $La_{9.5}(Ge_{5.5}Al_{0.5}O_{24})O_2$ (ref. 12) and is comparable to that of LSGM. The total conductivity of $La_{1.54}Sr_{0.46}Ga_3O_{7.27}$ between 600 and 800 °C is independent of oxygen partial pressure over the 1–10^{-27} atm range (Fig. 1e). Electromotive force measurements using an oxygen concentration cell showed an oxygen transport number of 0.9–0.95 (Fig. 1f) for $La_{1.54}Sr_{0.46}Ga_3O_{7.27}$. These data show that $La_{1.54}Sr_{0.46}Ga_3O_{7.27}$ is an oxide ion conductor with negligible electronic conduction. The temperature dependence of the conductivity in dry and wet O_2 flow from 200 to 1,000 °C is identical, which suggests that there is no proton conduction for this material and that protons are only minority defects.

To identify the mobile oxygen species, we collected constant-wavelength neutron diffraction data on $La_{1.54}Sr_{0.46}Ga_3O_{7.27}$ at ambient temperature on the BT1 diffractometer at NIST. Rietveld refinement, initially based on the structure of $LaSrGa_3O_7$ (ref. 19), gave $R_{wp} = 6.21\%$ and $\chi^2 = 1.89$ and showed that all of the sites in the framework were fully occupied, ruling out O and/or A site vacancies. Difference Fourier calculations showed positive scattering density around the 4e site (~0.33, ~0.17, ~0) between two A cations along the *c* axis. Refinement of an interstitial oxygen on this site gave an occupancy of 0.136(5) and significant improvement in the fit ($R_{wp} = 5.49\%$ and $\chi^2 = 1.48$). The interstitial oxygen O4 is located within the tetrahedral layers at the Ga1–Ga2 level in the pentagonal channels between the La/Sr cations (Fig. 2a,b). The refined total oxygen content of $O_{7.27(1)}$ per formula unit agrees well with that inferred from the cation composition. Refinement of anisotropic displacement parameters (ADPs) for all atoms significantly enhanced the fit ($R_{wp} = 4.76\%$ and $\chi^2 = 1.12$; see Supplementary Information, Fig. S10, Table S1), but the size and shape of the ellipsoids of several atoms (see Supplementary Information, Fig. S11) were consistent with positional disorder, presumably associated with structural relaxation around the interstitial oxygen, which appears underbonded (bond valence sum = 1.21) in this average structure. Thermogravimetric analysis (see Supplementary Information, Fig. S7), ICP (see Supplementary Information, Section 5) and infrared absorption data (see Supplementary Information, Fig. S9) excluded the possibility of water uptake or hydroxide anions to balance the bonding for O4. The ADPs of La/Sr and Ga2 (see Supplementary Information, Fig. S11) suggest that their local displacement towards O4 is the mechanism by which the structure overcomes this underbonding. The highly anisotropic displacement ellipsoids of O1 and O3 similarly indicate relaxation to remove the three short contacts (~2.2 Å) from interstitial O4 to the framework oxides.

A simple model for relaxation around the defect, involving those Ga2, La/Sr, O1 and O3 species neighbouring O4 being displaced to $(Ga2)_L$, $(La/Sr)_L$, $(O1)_L$ and $(O3)_L$ sites (Fig. 2d, Supplementary Information, Figs S11,S12, Tables S3–S5; $R_{wp} = 5.18\%$, and $\chi^2 = 1.32$) was refined. The resulting bulk structure and the local defect structure at the O4 interstitial oxygen are shown in Fig. 2c and d respectively. O4 is accommodated by the synergy of bonding geometry change at Ga2, modification of polyhedral internal and bridging angles and counterion displacement. The displacement of $(Ga2)_L$ towards O4 shortens this gallium–oxygen bond from 2.13(2) Å in the average structure to 1.81(2) Å, clearly showing that the interstitial O enters the coordination environment of one of the two distinct framework gallium centres. To form this bond, $(Ga2)_L$ displaces into a triangular face of the original tetrahedron (Fig. 2e) and incorporates O4 into one of the axial positions of the trigonal bipyramidal $(Ga2)_L$ coordination environment (Fig. 2f). The $(Ga2)_LO_5$ geometry is consistent with similar centres found in $Ga_2Te_4O_{11}$ (ref. 28) and some gallium phosphates[29]. This ability of the d^{10} Ga^{3+} cation to change coordination geometry is key to the stabilization of the oxygen interstitial. The associated displacement of O1, which is not in the coordination sphere of $(Ga2)_L$, to the $(O1)_L$ position relieves the close O4…O1 contact by changing the Ga2–O1–Ga2 bridge geometry and moves $(O1)_L$ towards one of the neighbouring pentagonal channel centres. The relaxation around O4 thus affects the geometry at all five Ga centres describing the pentagonal channel, and will disfavour interstitial occupancy of any of the five nearest-neighbour channel positions surrounding an occupied interstitial site. In addition to this formation of a new Ga–O bond, the displacement of the (La/Sr) counterions towards O4 electrostatically stabilizes

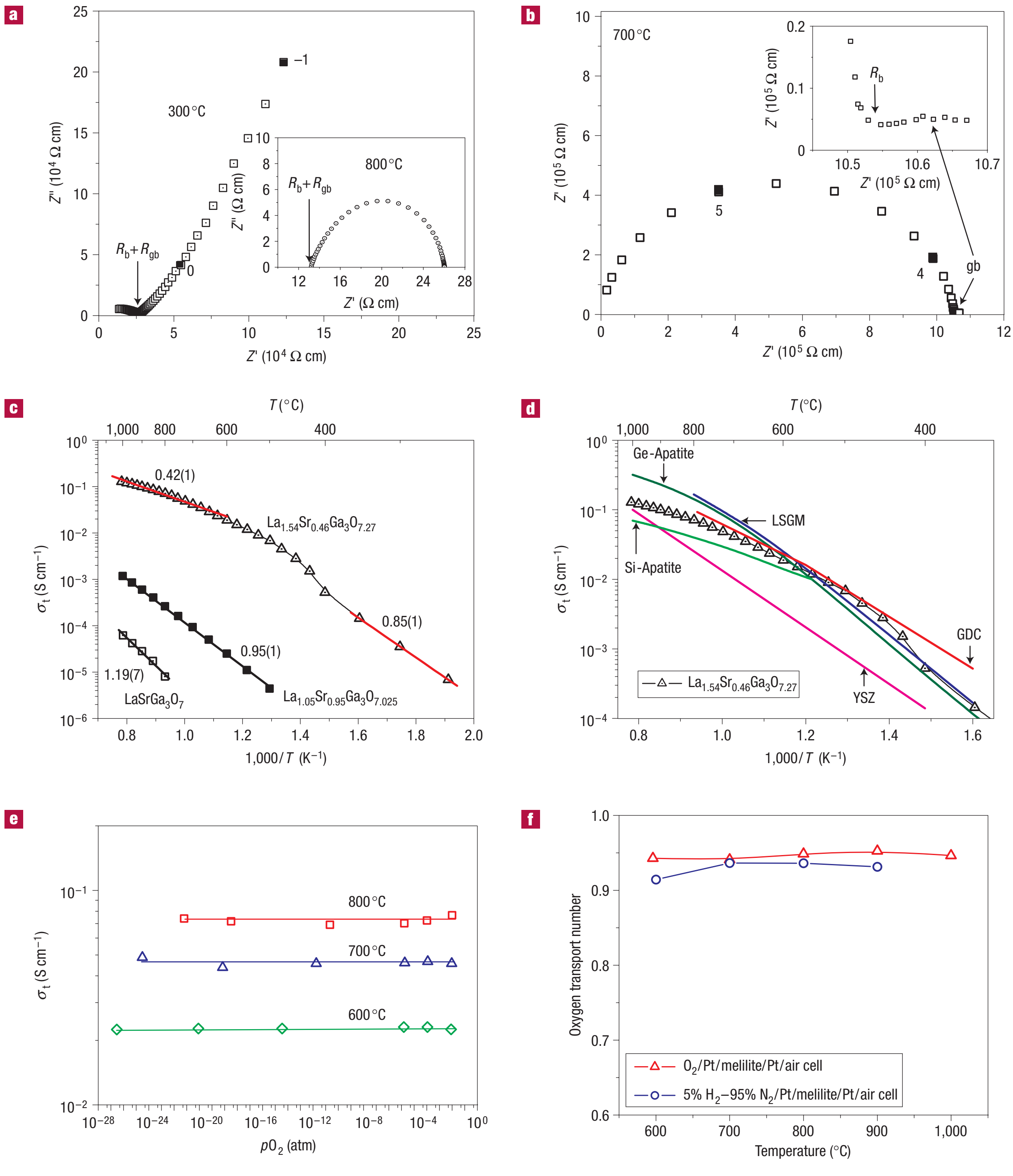

Figure 1 **Ionic conductivity of $La_{1.54}Sr_{0.46}Ga_3O_{7.27}$ (melilite). a**,**b**, Complex impedance plots of $La_{1.54}Sr_{0.46}Ga_3O_{7.27}$ (**a**) and the parent $LaSrGa_3O_7$ (**b**). **c**,**d**, Arrhenius plots. **e**, pO_2 dependence of total conductivity for $La_{1.54}Sr_{0.46}Ga_3O_{7.27}$. **f**, Oxygen transport number over the 600–1,000 °C range measured by the oxygen concentration cell method for $La_{1.54}Sr_{0.46}Ga_3O_{7.27}$. The numbers in **a**,**b** denote the frequency logarithms. In **b**, the parent $LaSrGa_3O_7$ shows insulating impedance behaviour, which comprises well-resolved insulating bulk (large semicircular arc) and grain boundary (gb) (small semicircular arc enlarged in the inset) responses. R_b and R_{gb} denote bulk and grain boundary resistivities, respectively. **c** shows the total conductivity of $La_{1.54}Sr_{0.46}Ga_3O_{7.27}$ compared with the parent $LaSrGa_3O_7$ and the lightly doped $La_{1.05}Sr_{0.95}Ga_3O_{7.025}$: activation energies (eV) are marked. **d** compares the total conductivity of $La_{1.54}Sr_{0.46}Ga_3O_{7.27}$ with current leading oxide ion electrolyte materials $La_{9.75}Sr_{0.25}(SiO_4)_6O_{2.895}$ (ref. 13) (Si-apatite), $La_{9.5}(Ge_{5.5}Al_{0.5}O_{24})O_2$ (ref. 12) (Ge-apatite), $Zr_{0.9}Y_{0.1}O_{1.95}$ (ref. 4) (YSZ), $La_{0.8}Sr_{0.2}Ga_{0.83}Mg_{0.17}O_{2.815}$ (ref. 20) (LSGM) and $Ce_{0.9}Gd_{0.1}O_{1.95}$ (ref. 27) (GDC).

the interstitial oxide, with the 2.39 Å contact the shortest to $(La/Sr)_L$ from all of the oxides in the structure. This cation displacement within the channels along the interlayer direction towards O4 is possible because of the lamellar nature of the structure. This model increases the O4 bond valence sum to 1.90 and provides a satisfactory description of the bonding around

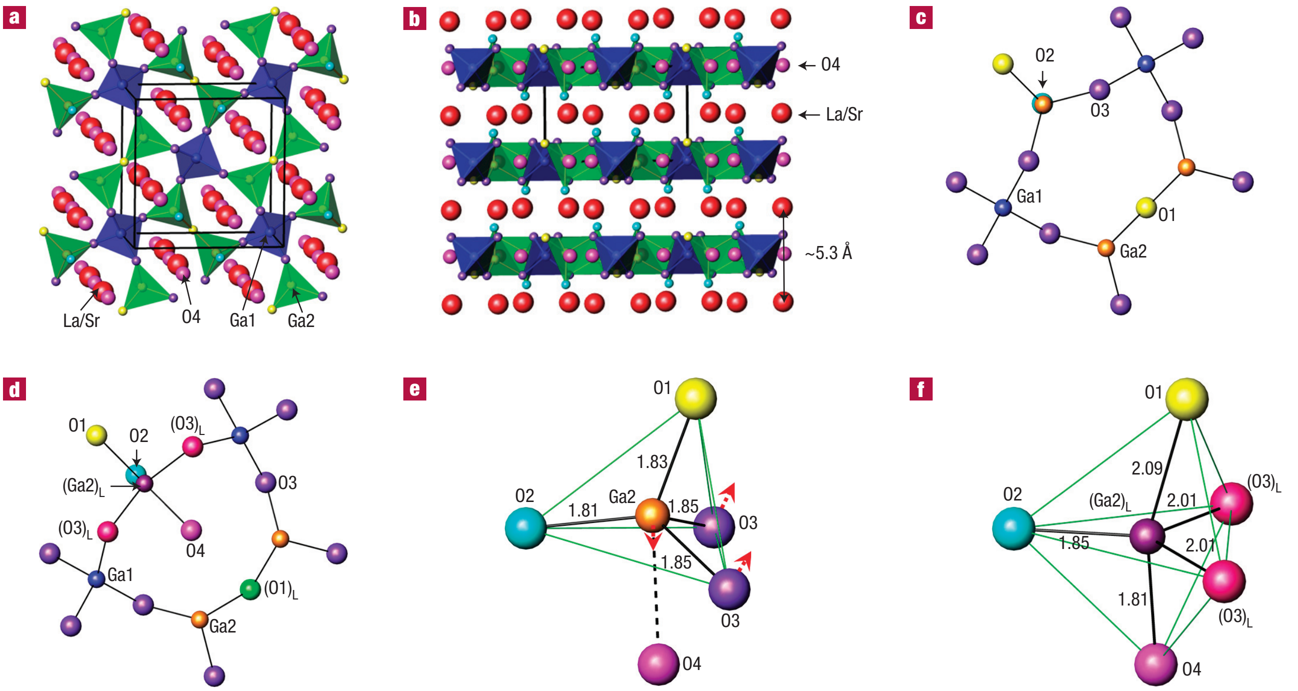

Figure 2 Structural relaxation around the interstitial oxide. Accommodation of oxygen interstitials in the melilite $La_{1.54}Sr_{0.46}Ga_3O_{7.27}$. **a**, 2D Ga_3O_7 corner-shared tetrahedral layers with La/Sr columns (red) and interstitial oxygen O4 (pink) located in the distorted pentagonal tunnels viewed along the *c*-axis direction. **b**, The stacking of the $(La/Sr)_2$ and Ga_3O_7 structural units along the *c* axis shows that the O4 interstitials are located in the Ga_3O_7 layers. The two distinct Ga-centred tetrahedra are distinguished by colouring—the fully condensed $(Ga1)O_4$ unit is shown in blue. **c**,**d**, The bulk structure (**c**) and local defect structure (**d**) around the oxygen interstitial O4. $(O1)_L$ is, unlike $(O3)_L$, not directly bound to $(Ga2)_L$ but relaxes away from interstitial O4, accommodated by a change in bond and bridging angles at Ga2. The O2 above the two Ga2 centres was omitted for clarity. **e**, The distortion of the $(Ga2)O_4$ tetrahedron (geometry taken from the parent undoped $LaSrGa_3O_7$ structure[19]; displacements marked with red arrows) involves motion of Ga2 into the face of the tetrahedron described by O2 and O3, which displaces to the relaxed $(O3)_L$ position to make the three equatorial oxides around $(Ga2)_L$ coplanar and remove a close O4…O3 contact. **f**, The resulting distorted trigonal bipyramidal $(Ga2)_LO_5$ polyhedron in the defect structure.

the defect. It reveals that displacements of up to 0.45 Å can take place within the 2D $Ga_3O_7^{5-}$ network to accommodate the interstitial anion.

Maximum-entropy method (MEM) analysis of the ambient-temperature neutron diffraction data, which minimizes bias imposed by the structural model, confirmed the existence of the oxygen interstitial by clearly showing scattering density at the 4e sites at the level of the gallate sheets in the tunnels (Fig. 3a,c and Supplementary Information, Fig. S14d). The extra scattering density around all of the atom sites is assigned to positional disorder associated with the local structural relaxations required to accommodate the interstitial oxygen.

The structural investigation shows that the interstitial oxygen located within the A cation tunnels at the level of the gallate sheets is responsible for the high oxide ion conductivity of $La_{1.54}Sr_{0.46}Ga_3O_{7.27}$, consistent with the conductivity increase over the parent $LaSrGa_3O_7$ and the lightly doped $La_{1.05}Sr_{0.95}Ga_3O_{7.025}$ by three and two orders of magnitude, respectively. $La_{1.54}Sr_{0.46}Ga_3O_{7.27}$ shows a curvature in the Arrhenius plot of the total conductivity at ∼400 °C (Fig. 1c). The activation energy (E_a) decreased from ∼0.85 eV for <400 °C to 0.42 eV over the 600–1,000 °C temperature range. Variable-temperature synchrotron X-ray diffraction (XRD) data from ambient temperature to 800 °C did not show evidence for a phase transition in $La_{1.54}Sr_{0.46}Ga_3O_{7.27}$, but nonlinear thermal expansion in the cell parameters of $La_{1.54}Sr_{0.46}Ga_3O_{7.27}$ is observed in the region of the conductivity anomalies (see Supplementary Information, Fig. S15). The nonlinear thermal expansion behaviour of the *c* axis for $La_{1.54}Sr_{0.46}Ga_3O_{7.27}$ thus coincides with the change in E_a, motivating analysis of the structure at high temperature.

Rietveld and MEM analyses of neutron diffraction data at a temperature (800 °C) where the oxygen interstitials are mobile revealed that the interstitial oxygen remains in the 4e sites in the tunnels with a similar local defect structure (see Supplementary Information, Tables S7–S9) to that observed at ambient temperature. The ADPs for O4 (see Supplementary Information, Table S6 from the average structure) are now extremely flattened within the layer (Fig. 4a; Supplementary Information, Fig. S13 shows a comparison between 800 °C and ambient temperature). This is reflected in a change in the O4 scattering density in the MEM analysis from spherical at ambient temperature to a half-moon shape at 800 °C (Fig. 3b,d). The highly anisotropic ADPs and scattering density for the interstitial oxygen at 800 °C suggest the diffusion of O4 is constrained within the Ga1–Ga2–O4 layers, consistent with the blockage of the pentagonal channels along the *c* axis by the La/Sr cations. At 800 °C, there is no continuous MEM scattering density distribution (see Supplementary Information, Fig. S14c) between the neighbouring O4 sites and between O4 and framework oxygen sites. This is consistent with a direct interstitial (single particle) mechanism for the oxygen diffusion rather than exchange between interstitial and framework oxygen. As each O4 site is surrounded by five nearest neighbours within the layer, the observed maximum interstitial content of <1/7 corresponds to all of the potential interstitial sites neighbouring a given O4 being empty. The O4 path to neighbouring sites is between the Ga centres defining the five

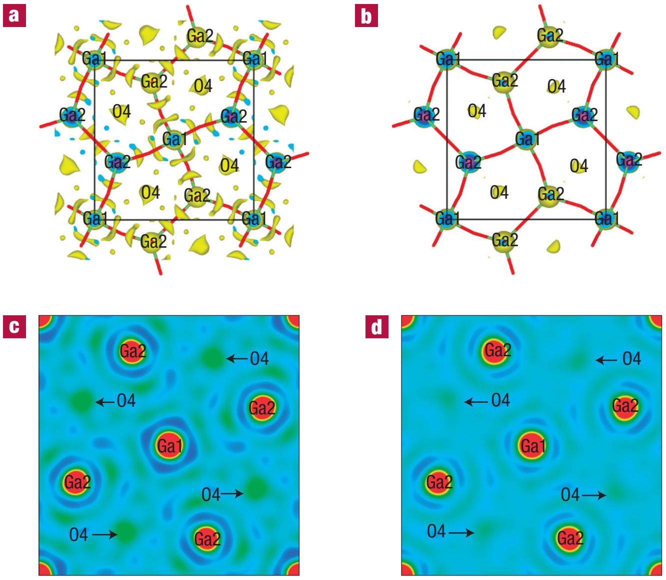

Figure 3 **Nuclear scattering density maps from MEM analysis for La$_{1.54}$Sr$_{0.46}$Ga$_3$O$_{7.27}$.** **a**,**b**, (001) projection at ambient temperature (**a**) and 800 °C (**b**) at the Ga1–Ga2–O4 level within a z range of -0.07–0.07 (isosurface level is 0.55 fm Å^{-3}). **c**,**d**, Scattering density distribution at the $z = 0$ section of the (001) plane at ambient temperature (**c**) and 800 °C (**d**). Scattering density from the interstitial oxygen O4 is marked with an arrow. The MEM scattering density is constrained by the site symmetry (for example, mirror symmetry at O4), whereas the ADPs have an artificial centre of symmetry superimposed. Supplementary Information, Fig. S14 shows the scattering density distribution at the $x = 0.33$ section of the (100) plane at ambient temperature (d) and 800 °C (e).

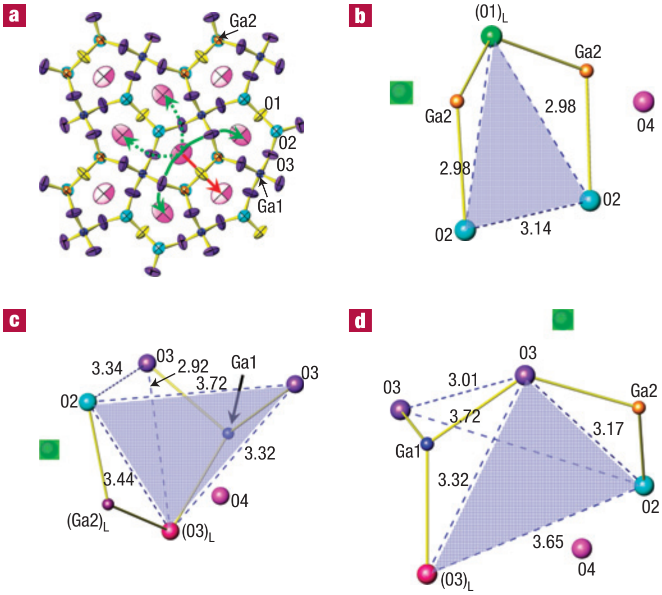

Figure 4 **Interstitial oxide migration pathways.** **a**, (001) view of displacement ellipsoid representation of La$_{1.54}$Sr$_{0.46}$Ga$_3$O$_{7.27}$ at 800 °C from the average structure model: four candidate interstitial O4 migration paths across the (O3, O3/O3$_{\mathrm{L}}$)–Ga1–O3/(O3)$_{\mathrm{L}}$–Ga2/(Ga2)$_{\mathrm{L}}$–O2 window are marked as green arrows (the broken arrow corresponds to the path over an Ga1–(Ga2)$_{\mathrm{L}}$ edge bridged by relaxed (O3)$_{\mathrm{L}}$ rather than the Ga1–Ga2 edge bridged by O3) and the one path across the O2–Ga2–(O1)$_{\mathrm{L}}$–Ga2–O2 edge as a red arrow. **b**–**d**, The windows on these edges separating near-neighbour O4 sites are shown for O2–Ga2–(O1)$_{\mathrm{L}}$–Ga2–O2 (**b**), (O3)$_2$–Ga1–(O3)$_{\mathrm{L}}$–(Ga2)$_{\mathrm{L}}$–O2 (**c**) and (O3, (O3)$_{\mathrm{L}}$)–Ga1–O3–Ga2–O2 (**d**). The vacant destination O4 sites are shaded with green squares. The ease of O4 motion across these paths is defined by the bottlenecks formed by these oxygen atom triangles: O2–(O1)$_{\mathrm{L}}$–O2 in the O2–Ga2–(O1)$_{\mathrm{L}}$–Ga2–O2 window; front and rear O3–(O3)$_{\mathrm{L}}$–O2 triangles in the (O3)$_2$–Ga1–(O3)$_{\mathrm{L}}$–(Ga2)$_{\mathrm{L}}$–O2 window and front (O3)$_{\mathrm{L}}$–O3–O2 triangle and rear O3–O3–O2 triangle in the (O3, (O3)$_{\mathrm{L}}$)–Ga1–O3–Ga2–O2 window. Front triangles are marked by hatching (the rear of the two triangles in **c** and **d** are unhatched) with the distances (Å) between each oxygen corner in the triangles. The largest space in the windows to permit the passage of O4 is via the circumcentres (defined as the point equidistant to all vertices) of these triangles, which have contacts to the framework O of ∼1.75 Å on the O2–Ga2–(O1)$_{\mathrm{L}}$–Ga2–O2 window, ∼2.02 Å (front triangle) and ∼1.88 Å (rear triangle) on the (O3)$_2$–Ga1–(O3)$_{\mathrm{L}}$–(Ga2)$_{\mathrm{L}}$–O2 window and ∼1.96 Å (front) and ∼1.94 Å (rear) on the (O3, (O3)$_{\mathrm{L}}$)–Ga1–O3–Ga2–O2 window.

edges of the pentagonal channel, passing over the bridging oxygen (O1/(O1)$_{\mathrm{L}}$ or O3/(O3)$_{\mathrm{L}}$). There are three different hopping paths (Fig. 4a) across the Ga2–Ga2, Ga1–Ga2 and Ga1–(Ga2)$_{\mathrm{L}}$ edges of the pentagonal channel; the narrowest points on these paths are windows described by three framework oxide anions (Fig. 4b–d). Consideration of the closest contacts to these window anions from the circumcentre of the window triangles (taken as the best representation of the O4 position in transit across the pentagon edge) reveals that the Ga2–Ga2 edge is more congested than the other two paths: the less favourable nature of hopping via the Ga2–(O1)$_{\mathrm{L}}$–Ga2 edge is apparent from the O4 ADP (Fig. 4a) and MEM density (Fig. 3b, Supplementary Information, S14c), which is clearly directed towards the other edges. The most favourable path is via the O3-bridged Ga1–Ga2 edge, which produces a 1.96 Å closest O4…O2/O3 approach on passing through the bottleneck from a static view of the structure, requiring dynamical opening of the windows to enable the O4 hop. Such cooperative movement of the framework oxygen is consistent with the enhanced anisotropy of both the refined displacement parameters (Fig. 4a) and the MEM-derived scattering density of all the framework oxygen atoms (see Supplementary Information, Fig. S14) compared with that at ambient temperature. The observed relaxation of up to 0.45 Å by atoms in the Ga$_3$O$_7$ net required to accommodate O4 in the static structure gives an estimate of the extent of local reorganization possible within the 2D tetrahedral framework—as O4 moves from one (Ga2)$_{\mathrm{L}}$ centre and pentagonal channel to a neighbour, relaxations of this size must occur to both return the structure of the original O4 site to that corresponding to an unoccupied channel and to relax the new channel. Dynamical relaxation of 0.45 Å by the window atoms as O4 passes would give closest O4…O (framework oxygen) contacts of an acceptable value of 2.41 Å. The proposed interstitial migration pathway thus requires physically sensible displacements to enable anion motion. The two close Ga–O4 distances (mean 1.85 Å) that arise when O4 is crossing the pentagon edges via the circumcentres of the triangular oxide windows are consistent with formation of intermediate edge-sharing Ga$_2$O$_9$ units (O$_4$Ga–O4–GaO$_4$). This would involve O4 becoming a bridging rather than a terminal oxygen between two five-coordinate Ga centres undergoing dynamically the type of static structural rearrangement found at (Ga2)$_{\mathrm{L}}$, forming an edge-sharing five-coordinate geometry found for O$_3$V$-$O$_2$–TeO$_3$ units in V$_4$Te$_4$O$_{18}$ (ref. 30).

The stability and mobility of oxygen interstitials in melilite can be assigned to the synergy of specific structural features. The 5.3 Å cation separation in the La/Sr cation chains running perpendicular to the 2D Ga$_3$O$_7^{5-}$ network provides sufficient space to accommodate the interstitial O, a role also played by the 7.2 Å separation between cations on the oxygen channel periphery in apatite (see Supplementary Information, Fig. S16). In both cases, the absence of 3D polyhedral connectivity enables electrostatic stabilization via relaxation of the countercations towards the extra anion, and the cation size enables it to increase its coordination number. The formation of a fifth Ga–O bond affords covalent stabilization of the interstitial oxide, requiring rearrangement of a polyhedron that forms part of an extended network. Such relaxation is straightforward for the '0D' isolated tetrahedra of apatite because none of the oxide anions is involved in, and thus constrained by, Si–O–Si bridging. It is the different structural roles of the two crystallographically distinct Ga-centred tetrahedra in the 2D layer (Fig. 2a) that give melilite the required flexibility—the tetrahedron centred on Ga1 is four-connected with all four oxygens bridging to other Ga tetrahedra, whereas that on Ga2 is three-connected and has a non-bridging terminal oxygen O2. The interstitial oxygen O4 thus binds solely to Ga2, which has the flexibility to reposition the terminal non-bridging oxide O2 in response. Binding at the Ga1 node would not be possible because of the enhanced constraints imposed by involvement of all the oxides defining this polyhedron in the formation of the layer. The mobility of the anion interstitials within the layer of corner-sharing tetrahedra is enabled by mechanisms closely related to those involved in relaxing the structure around the defect—flexibility of the windows connecting neighbouring sites arises from rotations and deformations of the gallium-centred polyhedra. Tetrahedral networks with non-bridging oxygens exhibit a high density of low-energy 'floppy modes'[31], consistent with the required deformations being particularly facile in melilite. The extent of dynamical relaxation required for the O4 charge carrier to move through the narrowest point between stable sites matches that found in the static structure around the defect, suggesting the formation of interstitial-bridged five-coordinate Ga sites as the anion crosses the pentagon edges.

Mobile interstitial oxides will be accessible in network-based materials families sharing the key crystal chemical features of melilite responsible for the high conductivity of $La_{1.54}Sr_{0.46}Ga_3O_{7.27}$. Structurally flexible components are a prerequisite for the accommodation of excess oxide—large electropositive cations can readily change coordination number, and the role of La^{3+} and Sr^{2+} in melilite is thus clear. Directionally bonded polyhedral complex anions enhance interstitial mobility by favouring more open structures than the close-packing found when large cations are combined with simple oxide anions. The corner-sharing gallium oxide tetrahedral network in melilite provides specific stabilization to the oxide interstitial by formation of a bond. This needs both a central element that can tolerate increased coordination number (ruling out P and S) and a mechanism to assimilate this local geometry change into the extended net. The key structural feature of melilite is the presence within the Ga_3O_7 sheet of the three-connected Ga2-based tetrahedral node with the non-bridging terminal oxide O2; this tetrahedron can respond with the structural flexibility characteristic of the isolated anions in apatite to bind the interstitial oxide to the polyhedral network. These terminal oxide ions can then be used to move beyond clearly favourable 0D examples such as apatite and identify partially condensed extended networks as candidate structure types for interstitial oxide conduction. Tetrahedral network candidates include 1D (Na_2SiO_3 (ref. 32) and $Ba_4Si_6O_{16}$ (ref. 33)) and 2D arrays, for example, three-connected $Na_2Si_2O_5$ (ref. 34), (3,4)-connected $Ba_2CuSi_2O_7$ (ref. 35), $Ca_2Zn(Ge_{1.75}Si_{0.25})O_7$ (ref. 35) and nordite $LaSrNa_3ZnSi_6O_{17}$ (ref. 36). 3D structures such as langasite ($La_3Ga_5SiO_{14}$) (ref. 37), which has fully condensed Si/Ga-based octahedra to give 3D connectivity but also the key terminal oxygens within the 2D silicate sheets, are also potential hosts. (Discussed structures are represented in Supplementary Information, Section 10.) Terminal oxygens are found in mixed polyhedral networks—fresnoite ($Ba_2TiSi_2O_8$) (ref. 38) has melilite-like five-rings with pyramidal Ti in the role of the four-connecting (Ga1-like) sites, whereas Si forms the three-connecting nodes, and could be replaced by elements more readily able to expand the coordination number; in $K_2MoAs_2O_9$ (ref. 39), the three-connected tetrahedral As plays the role of Ga2; La_2TiO_5 (ref. 40) has 1D pyramidal chains. The mobility of the stabilized interstitials is related to the flexibility of both the local coordination geometry and the extended structural motifs, so the materials above that duplicate both a structural (Ga1) and a flexible (Ga2) node as found in the melilite layer are particularly important. Interstitial mobility requires ready dynamical deformation of the framework—melilites adopt a range of incommensurate structures produced by long-range structural modulations arising from layer distortions enabled by such flexibility[41,42], and thus structure types containing terminal oxygens that exhibit incommensurate structures such as fresnoite[43] and $Na_2Si_3O_7$ (ref. 44) are important targets. The example of melilite suggests specific candidate structural families to accommodate mobile interstitial oxides—networks of variable-geometry complex polyhedral ions with relaxation-enabling terminal oxygens and large electropositive cations.

METHODS

SYNTHESIS

Phase relations of La_2O_3–SrO–Ga_2O_3 in the $La_{1+x}Sr_{1-x}Ga_3O_{7+\delta}$ range were investigated by solid-state reaction using La_2O_3 (99.999%, Alfa Aesar), $SrCO_3$ (99.995%, Aldrich) and Ga_2O_3 (99.999%, Alfa Aesar) as starting materials, which were mixed in ethanol and calcined at 1,200 °C for 12 h. After regrinding, the powders were uniaxially pressed into pellets and fired at 1,400 °C for 12 h. Single-phase samples of $La_{1.54}Sr_{0.46}Ga_3O_{7.27}$ were prepared by weighing starting materials according to the nominal composition $La_{1.54}Sr_{0.46}Ga_{3.05}$—the slight Ga excess ($\sim$1.7% mol) compensates for Ga volatilization during the high-temperature reaction. A 10 g batch of $La_{1.54}Sr_{0.46}Ga_3O_{7.27}$ for the neutron diffraction studies and dense pellet samples with 96% of the theoretical density for electrical measurements were made via cold-isostatic pressing with 30,000 psi pressure after being calcined at 1,200 °C for 12 h, followed by the final firing at 1,400 °C for 12 h. Prolonged firing for 24 h on one sample of $La_{1.54}Sr_{0.46}Ga_3O_{7.27}$ was carried out to check the phase evolution produced by Ga volatilization with the reaction time. Similarly, the phase-pure (by XRD) parent $LaSrGa_3O_7$ and slightly doped $La_{1.05}Sr_{0.95}Ga_3O_{7.025}$ (ref. 23) pellets for comparison on a.c. electrical conductivity with that for $La_{1.54}Sr_{0.46}Ga_3O_{7.27}$ were obtained via the use of a slight excess of Ga_2O_3 ($\sim$0.4 mol%) in the initial composition.

CHARACTERIZATION

The phase purity was checked by powder XRD data with a Panalytical X'pert Pro Multi-Purpose X-ray diffractometer (Co $K\alpha_1$ radiation $\lambda = 1.78901$ Å) and data for Rietveld refinement were collected over a 2θ range of 10–120°. Silicon was added as an internal standard during the laboratory XRD experiments to refine the cell parameter change with the composition.

a.c. impedance spectroscopy measurements in air from 250 to 1,000 °C were carried out with a Solartron 1255B Frequency Response Analyser, a Solartron 1296 dielectric interface and a Solartron 1287 electrochemical interface over the 10^{-2}–10^6 Hz frequency range. The a.c. conductivity as a function of partial oxygen pressure (pO_2) (monitored by a YSZ potentiometric sensor) was measured between 600 and 800 °C over a pO_2 range of 1–10^{-27} atm. The pO_2 value was controlled over the 1–10^{-4} atm pO_2 range by dilution of O_2 flow with Ar, for 10^{-4}–10^{-20} atm by using mixed 1%CO in Ar and 1%CO_2 in Ar flows and for less than 10^{-20} atm by 5%H_2 in N_2 flow. The dwell time at each pO_2 is 7–16 h ($\sim$7 h for $pO_2 > 10^{-4}$ atm and 12–16 h for $pO_2 < 10^{-4}$ atm) and continuous measurement was carried out to ensure equilibration of the samples with the gas environment at each point. Oxygen ion transport numbers were measured over 600–1,000 °C by using air–O_2 and 5% H_2 in N_2–O_2 gas concentration cells, using a double alumina tube described elsewhere[45]. The oxygen ion transport number was calculated from the ratio of the measured electromotive force from the Keithley 617 electrometer to the theoretical one from the Nernst equation using the ratio of pO_2 values. d.c. conductivity was measured using a four-probe set-up on a columnar sample bar in the 500–1,000 °C temperature range.

Variable-temperature synchrotron X-ray powder diffraction data from 20 to 800 °C were collected on station 9.1 at SRS on a sample diluted with quartz powder in a 0.7 mm quartz capillary at $\lambda = 0.802541$ Å. Constant-wavelength neutron diffraction data ($\lambda = 1.54030$ Å) were collected at ambient temperature and 800 °C on the BT1 diffractometer at NIST. Rietveld refinement was carried out using the GSAS package[46]. Whole-pattern fitting based on the MEM was carried out using the computer program PRIMA[47] with RIETAN-2000 (ref. 48), with 256 × 256 × 256 pixels. VESTA[49] was used to draw the nuclear density maps from the MEM analysis.

Compositional analysis was carried out by using energy-dispersive X-ray analysis on a JEOL 2000FX transmission electron microscope operated at 200 kV on 40 grains and by ICP optical emission spectroscopy, for which the samples were dissolved in a mixed HNO_3/HF solution at 50–100 °C. Hydrogen-reduction thermogravimetry was used to detect weight loss from Ga reduction and volatilization up to 800 °C. A ∼30 mg sample was placed in an alumina crucible and heated in a 5%H_2–95%N_2 flow with a ∼200 ml min^{-1} flow rate from ambient temperature to 800 °C with a heating rate of 10 °C min^{-1}. The thermogravimetric analysis–differential thermal analysis instrument (EXSTAR6000) was calibrated using ZrO_2 as the standard material. Infrared absorption data were collected using a Perkin Elmer RXI Fourier-transform infrared spectrometer at 4000–400 cm^{-1} on samples pressed with KBr. The microstructure of the $La_{1.54}Sr_{0.46}Ga_3O_{7.27}$ pellets was examined using a Hitachi S4800 scanning electron microscope. Before this examination, the pellet surface was polished, acid-etched with HNO_3 for 1 min, thermal-etched at 1,300 °C for 30 min and coated with gold to form a thin conducting layer.

Received 4 December 2007; accepted 17 April 2008; published 18 May 2008.

References

1. Steele, B. C. H. & Heinzel, A. Materials for fuel-cell technologies. *Nature* **414**, 345–352 (2001).
2. Goodenough, J. B. Oxide-ion electrolytes. *Ann. Rev. Mater. Res.* **33**, 91–128 (2003).
3. Boivin, J. C. & Mairesse, G. Recent material developments in fast oxide ion conductors. *Chem. Mater.* **10**, 2870–2888 (1998).
4. Lacorre, P., Goutenoire, F., Bohnke, O., Retoux, R. & Laligant, Y. Designing fast oxide-ion conductors based on $La_2Mo_2O_9$. *Nature* **404**, 856–858 (2000).
5. Boehm, E. *et al.* Oxygen transport properties of $La_2Ni_{1-x}Cu_xO_{4+\delta}$ mixed conducting oxides. *Solid State Sci.* **5**, 973–981 (2003).
6. Packer, R. J. *et al.* Lanthanum substituted $CeNbO_{4+\delta}$ scheelites: Mixed conductivity and structure at elevated temperatures. *J. Mater. Chem.* **16**, 3503–3511 (2006).
7. Yamamoto, A. *et al.* Rietveld analysis of the modulated structure in the superconducting oxide $Bi_2(Sr,Ca)_3Cu_2O_{8+x}$. *Phys. Rev. B* **42**, 4228–4239 (1990).
8. Allen, G. C., Tempest, P. A. & Tyler, J. W. Coordination model for the defect structure of hyperstoichiometric UO_{2+x} and U_4O_9. *Nature* **295**, 48–49 (1982).
9. Nakayama, S., Kageyama, T., Aono, H. & Sadaoka, Y. Ionic-conductivity of lanthanoid silicates, $Ln_{10}(SiO_4)_6O_3$ (Ln = La, Nd, Sm, Gd, Dy, Y, Ho, Er and Yb). *J. Mater. Chem.* **5**, 1801–1805 (1995).
10. Leon-Reina, L., Losilla, E. R., Martinez-Lara, M., Bruque, S. & Aranda, M. A. G. Interstitial oxygen conduction in lanthanum oxy-apatite electrolytes. *J. Mater. Chem.* **14**, 1142–1149 (2004).
11. Islam, M. S., Tolchard, J. R. & Slater, P. R. An apatite for fast oxide ion conduction. *Chem. Commun.* 1486–1487 (2003).
12. Leon-Reina, L. *et al.* High oxide ion conductivity in Al-doped germanium oxyapatite. *Chem. Mater.* **17**, 596–600 (2005).
13. Arikawa, H., Nishiguchi, H., Ishihara, T. & Takita, Y. Oxide ion conductivity in Sr-doped $La_{10}Ge_6O_{27}$ apatite oxide. *Solid State Ion.* **136**, 31–37 (2000).
14. Esaka, T., Minaai, T. & Iwahara, H. Oxide ion conduction in the solid-solution based on the scheelite-type oxide $PbWO_4$. *Solid State Ion.* **57**, 319–325 (1992).
15. Lacerda, M., Irvine, J. T. S., Glasser, F. P. & West, A. R. High oxide ion conductivity in $Ca_{12}Al_{14}O_{33}$. *Nature* **332**, 525–526 (1988).
16. Boysen, H., Lerch, M., Stys, A. & Senyshyn, A. Structure and oxygen mobility in mayenite ($Ca_{12}Al_{14}O_{33}$): A high-temperature neutron powder diffraction study. *Acta Crystallogr. B* **63**, 675–682 (2007).
17. Sansom, J. E. H., Tolchard, J. R., Islam, M. S., Apperley, D. & Slater, P. R. Solid state Si-29 NMR studies of apatite-type oxide ion conductors. *J. Mater. Chem.* **16**, 1410–1413 (2006).
18. Pramana, S. S., Klooster, W. T. & White, T. J. Framework 'interstitial' oxygen in $La_{10}(GeO_4)_5(GeO_5)O_2$ apatite electrolyte. *Acta Crystallogr. B* **63**, 597–602 (2007).
19. Skakle, J. M. S. & Herd, R. Crystal chemistry of $(RE,A)_2M_3O_7$ compounds (RE = Y, lanthanide; A = Ba, Sr, Ca; M = Al, Ga). *Powder Diffr.* **14**, 195–202 (1999).
20. Huang, K. Q., Tichy, R. S. & Goodenough, J. B. Superior perovskite oxide-ion conductor; strontium- and magnesium-doped $LaGaO_3$: I, phase relationships and electrical properties. *J. Am. Ceram. Soc.* **81**, 2565–2575 (1998).
21. Rozumek, M., Majewski, P., Sauter, L. & Aldinger, F. $La_{1+x}Sr_{1-x}Ga_3O_{7-\delta}$ melilite-type ceramics: Preparation, composition, and structure. *J. Am. Ceram. Soc.* **87**, 662–669 (2004).
22. Rozumek, M. *et al.* Electrical conduction behavior of $La_{1+x}Sr_{1-x}Ga_3O_{7-\delta}$ melilite-type ceramics. *J. Am. Ceram. Soc.* **87**, 1795–1798 (2004).
23. Raj, E. S., Skinner, S. J. & Kilner, J. A. Electrical conductivity, oxygen diffusion and surface exchange studies on a melilite-type $La_{1.05}Sr_{0.95}Ga_3O_{7+\delta}$. *Solid State Ion.* **176**, 1097–1101 (2005).
24. Macdonald, J. R. *Impedance Spectroscopy Emphasizing Solid Materials and Systems* (Wiley, New York, 1987).
25. West, A. R., Sinclair, D. C. & Hirose, N. Characterization of electrical materials, especially ferroelectrics by impedance spectroscopy. *Adv. Mater.* **1**, 65–71 (1997).
26. Tao, S. W. & Irvine, J. T. S. Preparation and characterisation of apatite-type lanthanum silicates by a sol–gel process. *Mater. Res. Bull.* **36**, 1245–1258 (2001).
27. Huang, K. Q., Feng, M. & Goodenough, J. B. Synthesis and electrical properties of dense $Ce_{0.9}Gd_{0.1}O_{1.95}$ ceramics. *J. Am. Ceram. Soc.* **81**, 357–362 (1998).
28. Dutreilh, M., Thomas, P., Champarnaud-Mesjard, J. C. & Frit, B. Crystal structure of a new gallium tellurite: $Ga_2Te_4O_{11}$. *Solid State Sci.* **3**, 423–431 (2001).
29. Guesdon, A., Monnin, Y. & Raveau, B. A sodium gallophosphate with an original tunnel structure: $NaGa_2(OH)(PO_4)_2$. *J. Solid State Chem.* **172**, 237–242 (2003).
30. Xiao, D. *et al.* Hydrothermal synthesis and crystal structure of a three-dimensional vanadium tellurite $V_4Te_4O_{18}$. *J. Solid State Chem.* **176**, 159–164 (2003).
31. Dove, M. T. *et al.* Floppy modes in crystalline and amorphous silicates. *Phys. Rev. Lett.* **78**, 1070–1073 (1997).
32. Liu, F., Garofalini, S. H., King-Smith, R. D. & Vanderbilt, D. Structural and electronic properties of sodium metasilicate. *Chem. Phys. Lett.* **215**, 401–404 (1993).
33. Hesse, K. F. & Liebau, F. Crystal-chemistry of silica-rich barium silicates.1. Refinement of the crystal-structures of $Ba_4[Si_6O_{16}]$, $Ba_5[Si_8O_{21}]$ and $Ba_6[Si_{10}O_{26}]$, silicates with triple, quadruple and quintuple chains. *Z. Kristallogr.* **153**, 3–17 (1980).
34. Fleet, M. E. & Henderson, G. S. Epsilon sodium silicate: A high-pressure layer structure $Na_2Si_2O_5$. *J. Solid State Chem.* **119**, 400–404 (1995).
35. Armbruster, T., Rothlisberger, F. & Seifert, F. Layer topology, stacking variation, and site distortion in melilite-related compounds in the system $CaO–ZnO–GeO_2–SiO_2$. *Am. Mineral.* **75**, 847–858 (1990).
36. Bakakin, V. V., Belov, N. V., Borisov, S. V. & Solovyeva, L. P. Crystal structure of nordite and its relationship to melilite and datolite-gadolinite. *Am. Mineral.* **55**, 1167 (1970).
37. Belokoneva, E. L., Stefanovich, S. Y., Pisarevskii, Y. V. & Mosunov, A. V. Refined structures of $La_3Ga_5SiO_{14}$ and $Pb_3Ga_2Ge_4O_{14}$ and the crystal-chemical regularities in the structure and properties of compounds of the langasite family. *Russ. J. Inorg. Chem.* **45**, 1642–1651 (2000).
38. Moore, P. B. & Louisnathan, J. Fresnoite: Unusal titanium coordination. *Science* **156**, 1361–1362 (1967).
39. Zid, M. F. & Jouini, T. $K_2MoO_2As_2O_7$. *Acta Crystallogr. C* **52**, 1334–1336 (1996).
40. Martin-Sedeno, M. C. *et al.* Structural and electrical investigation of oxide ion and proton conducting titanium cuspidines. *Chem. Mater.* **17**, 5989–5998 (2005).
41. Tamura, T. *et al.* Local structure of $(Ca,Sr)_2$ (Mg, Co, Zn) Si_2O_7 melilite solid-solution with modulated structure. *Phys. Chem. Min.* **23**, 81–88 (1996).
42. Jia, Z. H., Schaper, A. K., Massa, W., Treutmann, W. & Rager, H. Structure and phase transitions in $Ca_2CoSi_2O_7–Ca_2ZnSi_2O_7$ solid-solution crystals. *Acta Crystallogr. B* **62**, 547–555 (2006).
43. Hoche, T., Russel, C. & Neumann, W. Incommensurate modulations in $Ba_2TiSi_2O_8$, $Sr_2TiSi_2O_8$, and $Ba_2TiGe_2O_8$. *Solid State Commun.* **110**, 651–656 (1999).
44. Krueger, H., Kahlenberg, V. & Friese, K. $Na_2Si_3O_7$: An incommensurate structure with crenel-type modulation functions, refined from a twinned crystal. *Acta Crystallogr. B* **62**, 440–446 (2006).
45. Kuang, X. *et al.* Oxygen vacancy ordering phenomena in the mixed-conducting hexagonal perovskite $Ba_7Y_2Mn_3Ti_2O_{20}$. *Chem. Mater.* **19**, 2884–2893 (2007).
46. Larson, A. C. & Von Dreele, R. B. General Structure Analysis System (GSAS), Los Alamos National Laboratory Report LAUR 86-748 (2004).
47. Izumi, F. & Dilanian, R. A. *Recent Research Developments in Physics, Part II* Vol. 3, 699–726 (Transworld Research Network, Trivandrum, 2002).
48. Izumi, F. & Ikeda, T. A Rietveld-analysis programm RIETAN-98 and its applications to zeolites. *Mater. Sci. Forum* **321–324**, 198–203 (2000).
49. Momma, K. & Izumi, F. An integrated three-dimensional visualization system VESTA using wxWidgets. *Commission on Crystallogr. Comput., IUCr Newslett.* **7**, 106–119 (2006).

Supplementary Information accompanies this paper on www.nature.com/naturematerials.

Acknowledgements

We would like to thank Stephen Apter (Department of Chemistry, The University of Liverpool) for ICP elemental analysis, S. Poulton (NIST) for assistance with the neutron diffraction experiments and M. Roberts (SRS) for help with the synchrotron X-ray diffraction experiment. We thank EPSRC (EP/C511794) and the EU (FAME Network of Excellence) for support.

Author information

Reprints and permission information is available online at http://npg.nature.com/reprintsandpermissions. Correspondence and requests for materials should be addressed to M.J.R.